

Sapphire Photonic Crystal Waveguides for Terahertz Sensing in Aggressive Environments

Gleb M. Katyba,* Kirill I. Zaytsev,* Nikita V. Chernomyrdin, Irina A. Shikunova, Gennady A. Komandin, Vladimir B. Anzin, Sergey P. Lebedev, Igor E. Spektor, Valeriy E. Karasik, Stanislav O. Yurchenko, Igor V. Reshetov, Vladimir N. Kurlov,* and Maksim Skorobogatiy*

Terahertz (THz) frequency range opens significant opportunities in various fundamental and applied fields including condensed matter physics and chemistry, biology and medicine, public security and nondestructive testing. Despite significant advances in THz instrumentation, the problem of THz sensing in harsh environments, particularly at high temperatures and pressures, remains acute due to the lack of THz materials and optical components capable for operation under the extreme conditions. To address this problem, the THz hollow-core photonic crystal sapphire waveguides that are fabricated using shaped crystal growth technique are developed. Numerical analysis and experimental study show that the proposed waveguides operate in a few-mode regime and allow for the broadband transmission of THz pulses with small dispersions and low propagation losses. Thanks to the unique physical properties of sapphire, the proposed waveguides are capable of operating in a variety of aggressive environments. As an example, the developed waveguides are used to conduct the intra-waveguide interferometric sensing of phase transitions in sodium nitrite films at high temperatures. It is believed that the proposed sapphire-based material's platform has strong potential for developing THz guided optics for applications in intra-waveguide spectroscopy, interferometry, and remote sensing in aggressive environments.

nondestructive testing and imaging,^[10] and public security.^[11]

Most recently, THz frequency band was explored for applications in sensing and process monitoring in aggressive environments, which presents its own set of unique material and design requirements for the THz optics components and instrumentation. In these applications, using THz waveguides and fibers offer many benefits over the use of bulk optics. For example, application of the THz waves in medical diagnosis requires flexible radiation delivery to the hard-to-access tissues and internal organs, which can be effectively accomplished using slender THz fibers. At the same time, such fibers must be made of biofriendly materials, and they have to be resistant to the in vivo chemical composition of the biotissues.^[12] Similarly, application of the THz waves in monitoring of chemical reactions and phase transitions,^[13] diagnosis of plasmas,^[14] monitoring of processes in combustion engines,^[15] study of metal and alloy melts,^[16] all require waveguides

1. Introduction

Over the last decade, THz spectroscopy has been used with success in a variety of fundamental and practical applications,^[1,2] which among others include: spectroscopy of condensed matter^[3–5] and gases,^[6] medical diagnosis^[7,8] and therapy,^[9]

with advanced mechanical, chemical and thermal properties. Additionally, application of the THz waves in the open-space astrophysics^[17] requires THz waveguides featuring high radiation strength and resistance to the temperature fluctuations and gradients. In view of the many important practical and fundamental applications, there is a clear need for the durable

G. M. Katyba, Dr. I. A. Shikunova, Prof. V. N. Kurlov
Institute of Solid State Physics of RAS
Chernogolovka 142432, Russia
E-mail: katyba_gm@issp.ac.ru; kurlov@issp.ac.ru

G. M. Katyba, Dr. K. I. Zaytsev, N. V. Chernomyrdin,
Prof. V. E. Karasik, Dr. S. O. Yurchenko
Bauman Moscow State Technical University
Moscow 105005, Russia
E-mail: kirzay@gmail.com

 The ORCID identification number(s) for the author(s) of this article can be found under <https://doi.org/10.1002/adom.201800573>.

Dr. K. I. Zaytsev, N. V. Chernomyrdin, Dr. I. V. Reshetov, Prof. V. N. Kurlov
Sechenov First Moscow State Medical University
Moscow 119991, Russia

Dr. K. I. Zaytsev, N. V. Chernomyrdin, Prof. G. A. Komandin,
Dr. V. B. Anzin, Dr. S. P. Lebedev, Dr. I. E. Spektor
Prokhorov General Physics Institute of RAS
Moscow 119991, Russia

Prof. M. Skorobogatiy
Department of Engineering Physics
Polytechnique Montreal
2900 Boulevard Edouard-Montpetit, Montreal, Quebec H3T 1J4, Canada
E-mail: maksim.skorobogatiy@polymtl.ca

DOI: 10.1002/adom.201800573

and rugged THz waveguide capable of operating under extreme conditions.

Up to date, many types of waveguides have been developed for the THz frequency band. Thus, THz waveguides based on the hollow metal tubes^[18] or metal tubes with inner dielectric coatings,^[19] while having relatively low propagation losses, also feature significant intermodal dispersions, as well as low chemical resistance due to presence of the metallic layers in their structure. Various metallic plasmonic THz waveguides^[20–22] feature low loss and low dispersion, but they also suffer from low coupling efficiency, low chemical resistance, and they are difficult to handle. Plasmonic waveguides with highly-porous dielectric support^[23] are easier to handle, however, the resultant metal/dielectric structures lose some of their optical performance, while their metal and polymer components do not sustain aggressive chemicals, high temperatures and pressures. Alternatively, step-index dielectric THz waveguides made either of bulk crystalline materials^[24] or crystalline foams^[25] could be used in THz sensing in harsh environments, since some crystalline materials possess advanced chemical resistance and biocompatibility and are capable for operation at high temperatures and pressures. At the same time, a simple step-index geometry of these waveguides has a limited potential for reduction of the waveguide propagation losses and dispersion. Polymer microstructured, sub-wavelength, porous and multichannel waveguides,^[26–33] as well as antiresonant^[34–36] and photonic crystal (PC)^[37,38] waveguides allow efficient management of the waveguide dispersion and reduction of the propagation loss.^[39,40] While being suitable for the biomedical and chemical sensing due to their high flexibility, biocompatibility, and relatively high chemical resistance, the polymer THz waveguides are not adequate for sensing at high temperatures and pressures due to the polymer material's low mechanical strength and low melting point.^[41]

To address many challenges posed by the THz sensing in aggressive environments, in this paper, we have developed a novel hollow-core THz PC waveguide based on shaped sapphire crystals fabricated using the edge defined film-fed growth (EFG) technique.^[42,43] Sapphire material features many unique physical properties, such as high refractive index and relatively low electromagnetic wave absorption at THz frequencies,^[44] high hardness and melting point, chemical and radiation strength.^[45] In turn, the EFG-technique allows manufacturing high-quality shaped crystals with complex cross-sections directly from the Al₂O₃-melt.^[42] We, therefore, believe that the EFG-grown sapphire waveguides offer a powerful material's and fabrication platform to address even the toughest challenges in the THz sensing in aggressive environments.^[46]

In this work, several hollow-core PC waveguides of the same cross-section, but different lengths were grown using the EFG technique. Combining numerical analysis and experimental studies, we show that the sapphire waveguides considered in this paper operate in a few-mode regime. The two principal (lowest-loss) core guided modes of such waveguides have small dispersions of 0.06–1.0 ps (THz cm)⁻¹ in the frequency range of 0.65–1.2 THz, as well as low propagation losses 0.01–0.03 dB cm⁻¹ at 1.2 THz. We then applied the developed waveguides to the THz intra-waveguide interferometric sensing at high temperatures. Particularly, by using the waveguides

simultaneously as a cuvette and as an optical waveguide, we carried out a study of the phase transition in the sodium nitrite (NaNO₂) film.

2. Numerical Analysis of the Sapphire THz Waveguides

In this paper we use intra-waveguide interferometry to sense temperature-induced changes in the refractive index of a material. The THz waveguides used in the intra-waveguide interferometry setup should support at least two core-guided modes featuring small dispersions and low propagation losses. Moreover, effective refractive indexes of the two modes should have significantly different sensitivities to optical changes in the analyte layer placed in the waveguide core. This can be achieved by ensuring that the field distributions of the two modes have significantly different overlaps with the analyte layer.

In order to develop a sapphire waveguide with the modal properties favorable for the intra-waveguide interferometry, we optimized the waveguide geometry using the commercial finite-difference software Lumerical Mode Solutions,^[47] while taking into account various technological limits posed by the EFG technique. Bulk optical properties of sapphire in the THz region were taken from ref. [44] assuming that the crystal *c*-axis is directed along the waveguide direction. In our simulations, we accounted for the sapphire birefringence by using the property defined dielectric tensor, however, we did not observe a significant impact of the crystal birefringence on the core-guided mode optical properties. This is due to strong localization of the core-guided modes in the large-diameter hollow core.

In **Figure 1a** we present schematic of the THz sapphire waveguide optimized for the intra-waveguide interferometry sensing. The waveguide features an outer diameter of $D_O = 24.0$ mm, and a large central channel (core) with a diameter of $D_C = 7.15$ mm. The core is surrounded with smaller channels of diameter $d = 1.6$ mm. These channels are placed in the vertices of a hexagonal lattice with a period of $\Lambda = 2.8$ mm, thus forming two layers of the PC cladding.

In **Figure 1b**, we present numerically computed effective refractive indices n_{eff} of the core modes guided via bandgap effect (in blue-to-red), as well as antiresonant cladding modes and the modes of a continuum (in gray) that are mostly confined in the finite-size waveguide cladding. The core-bound bandgap-guided modes were differentiated from the antiresonant cladding modes by comparing them to the modes of a corresponding waveguide with an infinite PC cladding. We use blue-to-red and grayscale colorbars to indicate losses of the two types of waveguide modes. From **Figure 1b**, we notice that the antiresonant cladding modes are most abundant at frequencies below 0.5 THz, while most of the bandgap guided modes are observed at higher frequencies of 0.5–1.2 THz.

Among all the bandgap-guided modes, we note, in particular, the two lowest-loss core-guided modes, which are also the closest to the air light line ($n_{\text{eff}} = 1$). Propagation losses of these two modes are several times lower than losses of all the other core-guided modes, therefore, the two modes will play the predominant role in the intra-waveguide interferometry. Using analogy with the core-guided modes of the hollow-core circular

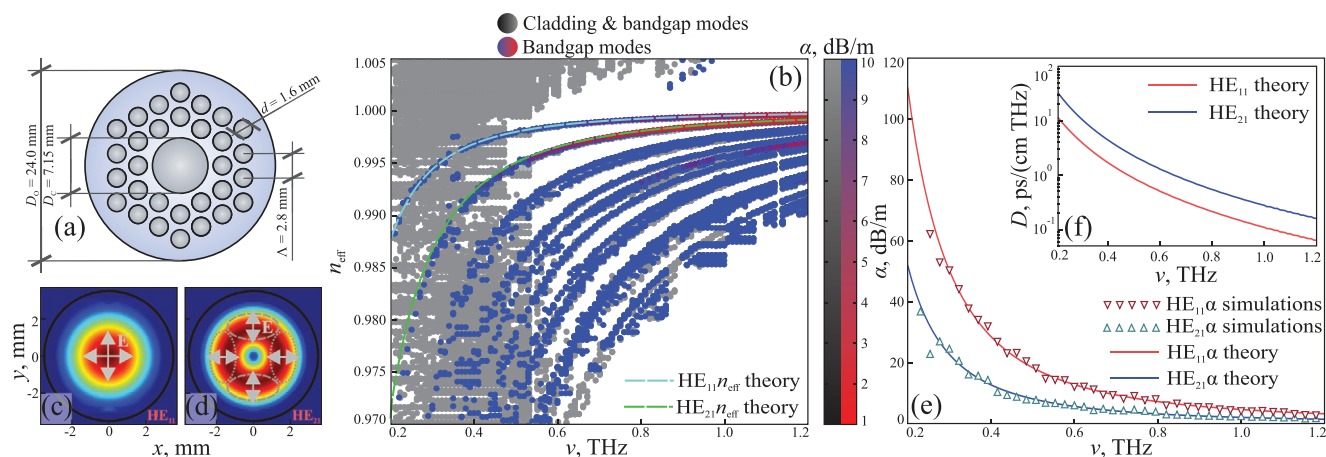


Figure 1. Numerical analysis of the THz-wave propagation in the hollow-core sapphire PC waveguide: a) waveguide geometry and b) effective refractive indices n_{eff} of the bandgap-guided core modes (red–blue colorbar), as well as antiresonant cladding modes and the modes of a continuum (gray-scale colorbar). c,d) Intensity distributions $I \propto |E|^2$ of the HE_{11} -like and HE_{21} -like modes at 1.1 THz. e,f) Modal losses α and modal dispersions D of the HE_{11} -like and HE_{21} -like modes. In (b), (e), and (f), solid lines correspond to the analytical fits of n_{eff} , α , and D using analytical dispersion relation in the form given by Equation (1).

Bragg fibers,^[48] we recognize that the two lowest-loss modes of the hollow-core sapphire PC waveguides studied in this work are similar to the fundamental HE_{11} mode, and the higher-order HE_{21} ring mode of the Bragg fibers. In Figure 1c,d, we show intensities $I \propto |E|^2$ of the HE_{11} -like and HE_{21} -like modes of the hollow-core sapphire PC waveguide at 1.1 THz. Furthermore, we note that in the frequency range of 0.65–1.2 THz the dispersions of the two modes vary in the interval of 0.06–1.0 ps (THz cm)⁻¹, while modal losses are lower than 0.1 dB cm⁻¹ in the whole frequency range, and becoming as low as 0.03–0.01 dB/cm⁻¹ at 1.2 THz.

In Figure 1b, we also present analytical fits of the effective refractive indices n_{eff} , losses α , and dispersions D of the two modes (solid lines) using the following fitting functions

$$\begin{aligned} n_{\text{eff}} &= n_{\text{eff}}^{\text{R}} - in_{\text{eff}}^{\text{I}} \\ n_{\text{eff}}^2 &= 1 - \frac{v_{\text{A}}^2}{v^2 - iv_{\text{B}}v} \\ \alpha &= \frac{4\pi v}{c_0} n_{\text{eff}}^{\text{I}} \\ D &= \frac{1}{c_0} \frac{\partial^2 (n_{\text{eff}}^{\text{R}} \omega)}{\partial \omega^2} \end{aligned} \quad (1)$$

where $c_0 = 2.998 \times 10^8$ m s⁻¹ is a speed of light in the free space, v is the electromagnetic wave frequency, v_{A} and v_{B} are the model fitting parameters with the units of frequency [Hz], and α is the modal intensity loss. This convenient parametrization of the modal complex dispersion relation has the Lorentian form,^[49] thus, obeying the Kramers–Kronig relations, as required from the response-function of a physical system.^[50] For the fundamental HE_{11} mode, and the higher-order HE_{21} ring mode the fitting parameters are found to be $v_{\text{A},\text{F}} = 0.0323$ THz, $v_{\text{B},\text{F}} = 0.0486$ THz, and $v_{\text{A},\text{HO}} = 0.0511$ THz, $v_{\text{B},\text{HO}} = 0.0085$ THz.

It should be noted that HE_{21} mode has an “odd” symmetry, which implied that it can be excited only using an off-centered linearly polarized Gaussian-like THz beam. Indeed, during

waveguide characterization, we use an off-center excitation that was optimized to result in the sharpest pattern of two-mode interference.

3. Fabrication of the Sapphire THz Waveguides

High hardness of sapphire and significant anisotropy of its physical properties^[45] make it impossible to produce microstructured crystals (such as the one shown in Figure 1a) using mechanical processing of bulk crystals. Alternatively, numerous approaches for the growth of shaped crystals directly from the melt were developed over the past decades^[42] using variants of the EFG technique.

In this work, we used the EFG technique to fabricate sapphire waveguide shown in Figure 1a. **Figure 2a** shows schematic of the growing process. The sapphire crystal is grown from the Al_2O_3 -melt meniscus that is formed at the top of a custom-made capillary die. During the growth, the melt rises to the top of the die through the ring capillary channels, while the crystal cross-section is defined by the die geometry. The detailed description of the EFG-growth setup is presented in the Experimental Section of the paper.

In this work, we produced several waveguide samples of various lengths employing either single- or double-seeding approaches. Both approaches provide shaped crystals of the desired cross-section, however, double-seeding reduces the length of crystal enlargement and eliminates large-scale bending of the shaped crystal, which could happen when using single-seeding. In Figure 2d, we show the 100 and 150 mm length sapphire THz waveguides. In Figure 2e, we also notice inclusions of the gas microbubbles (predominantly, Ar) between the first and the second layers of the cladding channels in the waveguide cross-section. These bubbles are located where the two melt flows moving from the peripheral and the central ring capillary channels meet each other.^[51] These bubbles can, in principle, locally decrease the material refractive index and affect the guiding properties of the shaped crystal,

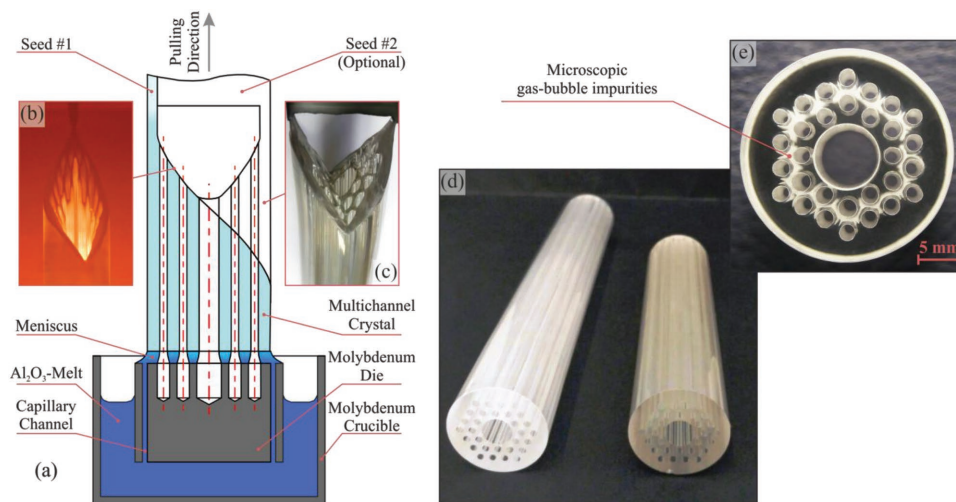


Figure 2. Fabrication of the sapphire THz PC waveguides using the EFG technique: a) schematics of a single-seed (Seed #1) and a double-seed (Seed #2) growth processes. b) In situ photo of the waveguide growth using single-seeding, c) photo of the as-grown waveguide using double-seeding, d) as-grown waveguides with the lengths of 100 and 150 mm, and e) photo of the waveguide cross-section.

however, these effects are difficult to quantify at this time and more investigations are in order.

4. Optical Characterization of the Sapphire THz Waveguides

We applied transmission-mode THz time-domain spectroscopy (THz-TDS)^[1] to conduct optical characterization of the fabricated sapphire waveguides. Detailed description of the experimental setup and measurement process is presented in the Experimental Section.

In **Figure 3a**, we show the THz spectra $|E(\nu)|$ of the reference and transmitted THz signals, both for 100 and 150 mm length waveguides. We should comment on the selection of these two waveguide lengths for the experimental study. First, the length should be long enough to filter out higher order modes, so only two lowest-loss modes remain in the waveguide. At the same time, if the waveguide is too long, only a single lowest loss

mode will remain, again, precluding using the waveguide for the intra-waveguide interferometry experiments. Considering these two limitations, and using theoretical data for the modal losses from our numerical simulations, we concluded that ideal length of a two-mode waveguide should be at least 50–100 mm and no longer than 200–300 mm. During measurements, we adjust the waveguide position in order to achieve the sharpest interference pattern in the frequency domain. To achieve this, we use the off-centered THz pumping in order to excite both “even” HE_{11} and “odd” HE_{21} modes in the waveguide core. By normalizing the waveguide transmission spectra to the reference one, we then calculate the waveguide transmission spectra $T_{\text{exp}}(\nu)$ (see **Figure 3b,c**). As compared to the relatively featureless reference THz spectrum, the spectra of the signals transmitted through the two waveguides feature periodic modulations due to the intra-waveguide interference phenomenon. Particularly, at certain frequencies, constructive interference of the principle core-guided modes leads to higher THz wave transmission through a waveguide. The modulation patterns

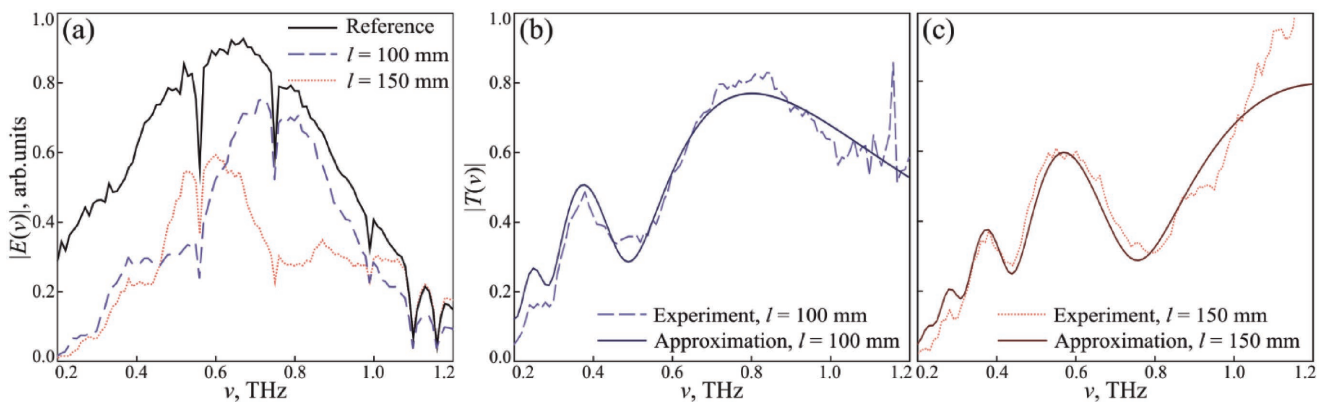


Figure 3. Optical characterization of the hollow-core sapphire THz PC waveguides: a) spectra of the THz reference and the THz-signals transmitted through the 100 and 150 mm long waveguides. b,c) Comparison between experimental and analytically fitted (using Equations (1) and (2)) spectra $|T(\nu)|$ for the two waveguides of lengths 100 and 150 mm.

are different for the waveguides of different lengths, and they cannot be observed if only a single-mode is excited.

A direct reconstruction of the effective modal refractive indices n_{eff} and the propagation losses α for both HE₁₁ and HE₂₁ modes from the transmission-mode spectroscopy data is a daunting task. In order to solve this inverse problem, we applied a model-based reconstruction of n_{eff} and α for the two modes following the approach detailed in ref. [52]. To explain experimental waveguide transmission data, we use analytical model that assumes a coherent superposition of the two core-guided modes featuring two distinct complex amplitudes and two distinct complex dispersion relations

$$T_{\text{th}} = C_{\text{F}} \exp(-i\varphi_{\text{F}}) \exp\left(-i \frac{2\pi\nu}{c_0} n_{\text{eff,F}} l - \alpha_{\text{F}} l\right) + C_{\text{HO}} \exp(-i\varphi_{\text{HO}}) \exp\left(-i \frac{2\pi\nu}{c_0} n_{\text{eff,HO}} l - \alpha_{\text{HO}} l\right) \quad (2)$$

where l is a waveguide length, $n_{\text{eff,F}}$, $n_{\text{eff,HO}}$, α_{F} , α_{HO} are the effective refractive indices and losses of the fundamental HE₁₁ and the higher-order HE₂₁ modes in the parametric form given by Equation (1), where we use the parameter values found using numerical simulations discussed earlier. In this model, the complex coefficients $C_{\text{F}} \exp(-i\varphi_{\text{F}})$ and $C_{\text{HO}} \exp(-i\varphi_{\text{HO}})$ define the net effect of the modal in- and out-coupling, which vary both in amplitude and phase from one mode to another. In principle, these coefficients have a frequency-dependent character, however, in this work, for simplicity, we assume that they are constant across the whole frequency range.

In order to fit the experimental transmission data using the model defined by Equation (2) and dispersion relations in the parametric form Equation (1), we need to specify 8 frequency-independent parameters – $\nu_{\text{A,F}}$, $\nu_{\text{B,F}}$, C_{F} , φ_{F} for the fundamental mode HE₁₁ and $\nu_{\text{A,HO}}$, $\nu_{\text{B,HO}}$, C_{HO} , φ_{HO} for the higher-order mode HE₂₁. In order to find these parameters, we used the least squares minimization of the frequency-averaged difference between the complex transmission spectra T_{exp} and T_{th} using the data for both the 100 and 150 mm long waveguides. Particularly, we minimize the following weighting function

$$\Phi = \frac{1}{N_{\nu}} \sum_{\nu_{\text{min}}}^{\nu_{\text{max}}} \frac{1}{N_l} \sum_{l=1,2} |T_{\text{exp}}(\nu, l) - T_{\text{th}}(\nu, l)|^2 \quad (3)$$

where N_{ν} and N_l stand for the number of the frequency points and the waveguide lengths, used in the fitting.

In Figure 3b,c, we compare experimental spectra (dashed curves) and their analytical fits (solid curves) for the waveguides of two different lengths. We note that the beating patterns between the two core-guide modes are very well reproduced across the whole spectral range for both waveguides. In Figure 4, we also compare two sets of the modal parameters, one obtained by fitting the numerical mode solver data described in Section 2, while the other one is obtained by fitting the experimental transmission spectra described in this section. A very good agreement is found between the two data sets, thus confirming effectively two-mode nature of the THz wave propagation through the fabricated hollow-core sapphire THz PC waveguides. Finally, we find that both HE₁₁-like and HE₂₁-like

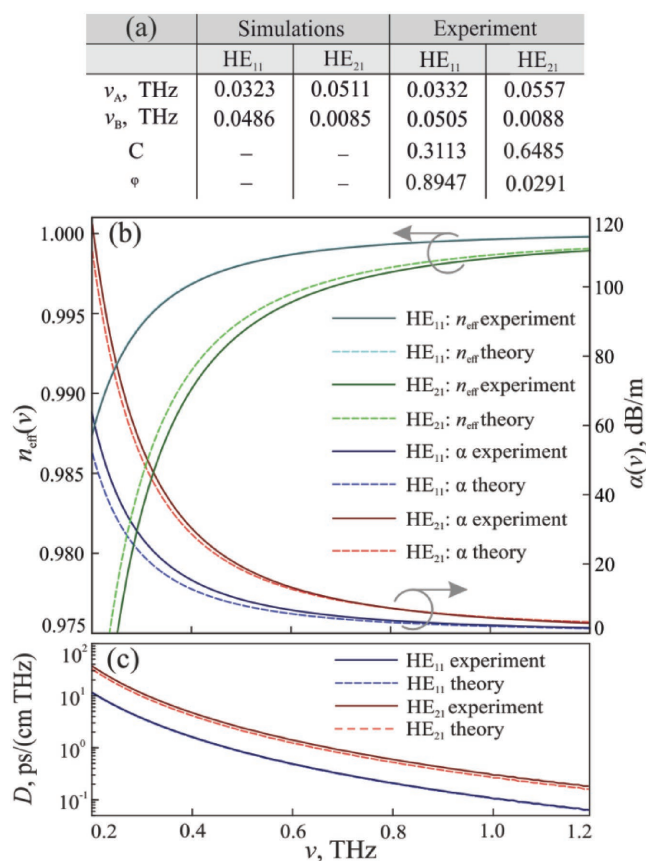


Figure 4. Modal properties of the fundamental HE₁₁-like and the higher order HE₂₁-like guided modes, comparison between the two sets of parameters/curves. One set is obtained by fitting the numerical mode solver data described in Section 2 (labeled theory), while the other one is obtained by fitting the experimental transmission spectra described in Section 4 (labeled experiment). a) Table of the fitting parameters used in the analytical dispersion relations (Equation (1)). b) Corresponding effective refractive indices n_{eff} and propagation losses α of the two principle guided modes. c) Corresponding dispersions D of the two guides modes.

guided modes feature low dispersion and losses, as predicted by the numerical study of Section 2.

5. High-Temperature THz Intra-Waveguide Interferometric Sensing

To demonstrate potential of the sapphire waveguides for applications in aggressive environments, we apply them to high-temperature intra-waveguide sensing of phase transition in NaNO₂—a pale yellow crystalline powder, which is highly soluble in water, hygroscopic, and serves as a precursor for production of a variety of organic compounds.^[53]

In Figure 5a, we show schematic of the THz intra-waveguide interferometry setup that uses the backward wave oscillator (BWO) and the Golay cell as a continuous-wave source and a detector of the THz radiation^[1] (for more details see the Experimental section). Our setup is optimized for the simultaneous excitation of the two core-guided HE₁₁-like and HE₂₁-like modes

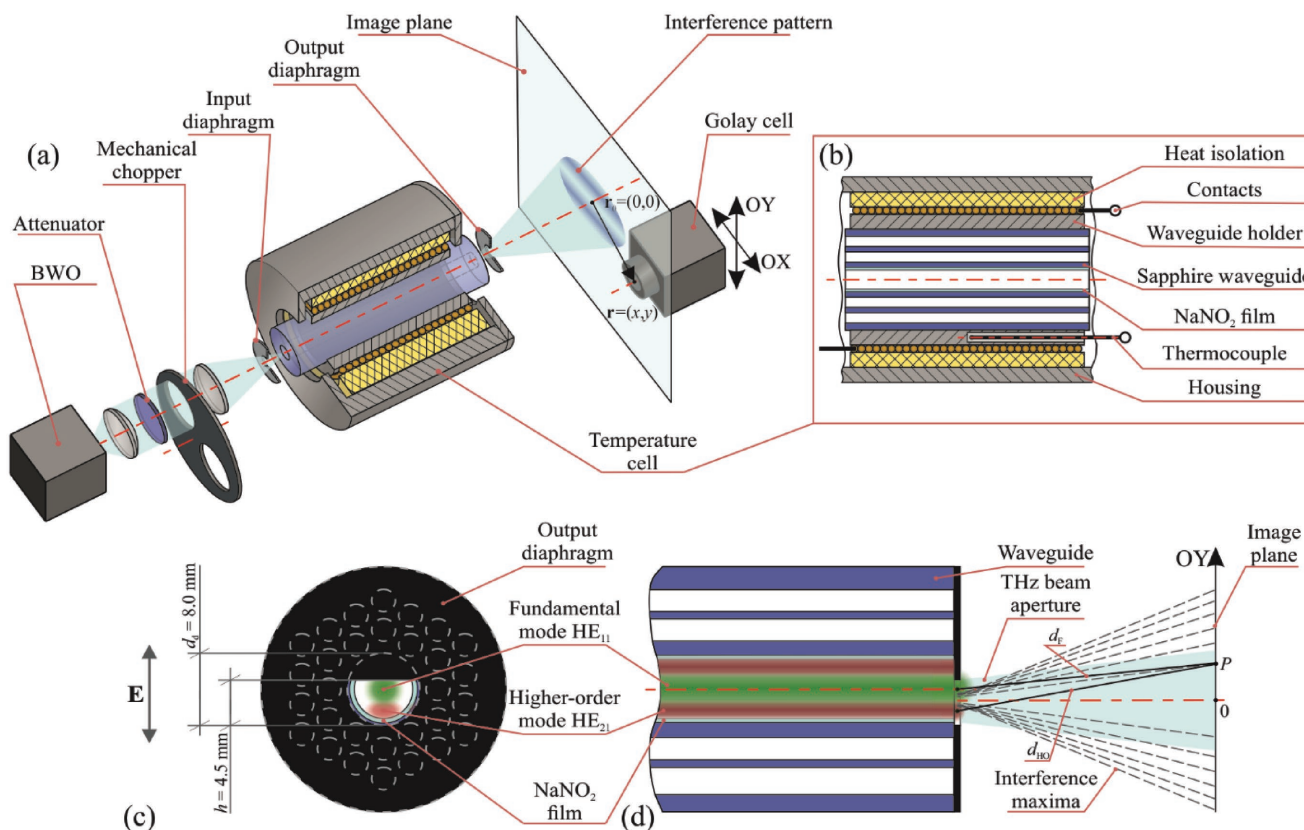


Figure 5. High-temperature THz intra-waveguide interferometry: a) schematic of the transmission-mode interferometry setup, b) schematic of the sapphire waveguide, mounted inside a temperature cell and containing NaNO₂ film in the central channel, c) schematic of the nonsymmetric output diaphragm, placed at the output end of the waveguide for the interference pattern formation by the fundamental mode HE₁₁ and the bottom part of the higher-order mode HE₂₁, d) schematic of the interference pattern formation, where the gray dashed lines indicate the directions of the interference pattern maxima.

via the off-center waveguide launch, which results in the high-contrast two-mode interference pattern at the waveguide output end (see Figure 5b). The interferogram evolves when the temperature changes. By comparing the temperature evolutions of the two interferograms, one with an analyte and another without an analyte, one can detect phase changes in the tested material. In order to enhance the interferogram contrast, we also cover the output end of a waveguide with a diaphragm in the form of a half-opened disk (see Figure 5c) with a diameter of $d_d = 8.0$ mm and an opening size of $h = 4.5$ mm. This is necessary as the two modes are of different symmetry. As shown in Figure 5d, the resultant interference pattern features several horizontal stripes formed by the constructive interference between the fundamental mode HE₁₁ and the lower part of the higher-order HE₂₁ mode.

As seen from Figure 5d, locations of the interference pattern maxima can be found from the constructive interference condition

$$d_F - d_{HO} + (n_{\text{eff},F} - n_{\text{eff},HO})l + \varphi_0 = m\lambda \quad (4)$$

where $n_{\text{eff},F}$ and $n_{\text{eff},HO}$ are the effective refractive indices of the two core modes, l is a waveguide length, λ is a wavelength of the guided light, m is an integer, d_F and d_{HO} are the distances between the observation point P and the points of the maximal

intensity of the HE₁₁-like and HE₂₁-like modes in the output diaphragm plane, while φ_0 is a constant phase shift between the two core-guided modes accrued during excitation. As follows from Equation (4), any environmental factor that affects differently the two guided mode effective refractive indices $n_{\text{eff},F}$ and $n_{\text{eff},HO}$, will lead to changes in the interference pattern. This is a principal idea behind the intra-waveguide interferometric sensing.

As a demonstration, we perform the intra-waveguide interferometric sensing of changes in the NaNO₂-film optical properties as a function of temperature. In this measurement, the analyte film is first deposited inside of the hollow waveguide core. Particularly, 20 mg of the NaNO₂-powder was first dissolved in distilled water. Then, some of the aqueous solution was injected into the core and evenly distributed along its length. After evaporation of water from the solution, a polycrystalline solid NaNO₂-film was formed at the bottom of the core. The process was then repeated several times for various orientations of the waveguide core in order to increase the sensor sensitivity.

In Figure 6, we show results of the high-temperature THz intra-waveguide interferometric measurements at 0.355 THz, where we compare waveguide with a NaNO₂ film to an empty one. The interference patterns $I(\mathbf{r})$ (where \mathbf{r} is a radius vector in the image plane) were recorded at the image plane for several

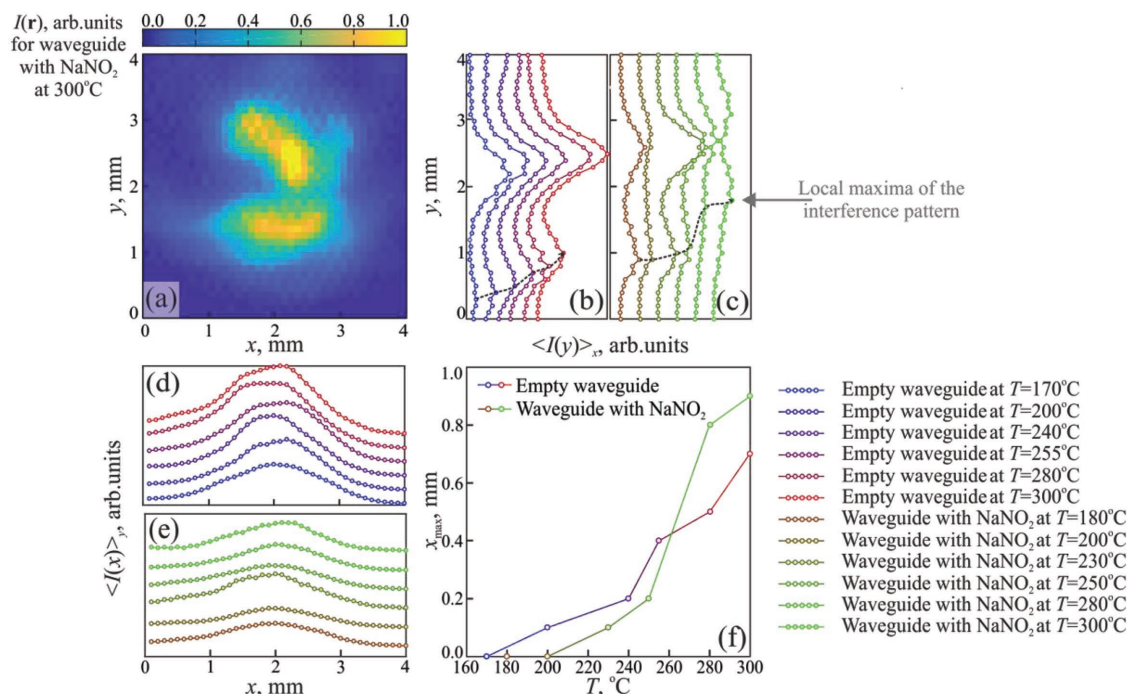


Figure 6. THz intra-waveguide interferometry of the NaNO₂-film at 0.355 THz: a) an interferogram $I(\mathbf{r})$ at the output of the 150 mm long waveguide containing NaNO₂-film at 300 °C. b,c) A “waterfall” plot of the spatially averaged (along the OX direction) interferogram $\langle I(y) \rangle_x$ for the empty (blue-to-red), and the NaNO₂-impregnated (brown-to-green) waveguides. d,e) A corresponding plot for the interferogram averaged along the OY direction $\langle I(x) \rangle_y$. f) Position of the lower interference fringe along in the OY-direction for the empty (blue-to-red) and the NaNO₂-impregnated (brown-to-green) waveguides.

temperature values in the range of 170–300 °C. In Figure 6a, we show $I(\mathbf{r})$ for the 150 mm long waveguide with a NaNO₂ film at 300 °C; as expected, the interference pattern features several stripes along the OX direction. In Figure 6b,c, we use a “waterfall” plot to illustrate changes in the interference patterns as a function of temperature for a waveguide with a NaNO₂ film and an empty one. Here we plot the averaged intensity $\langle I(y) \rangle_x$ along the OX direction. We note that all the interference patterns have two maxima, the position and the contrast of which vary with the temperature in a different manner depending whether the waveguide contains a NaNO₂ layer or not. For a waveguide with an analyte layer, the positions of the local interference fringes in the OY direction change significantly in the 250–280 °C temperature range compared to an empty waveguide, thus signaling the onset of the material phase change. By contrast, in Figure 6d,e, we show the averaged intensity $\langle I(x) \rangle_y$ along the OY direction that feature close-to-symmetric shapes in the OX direction and unremarkable changes with temperature. In (b)–(e), averaging of the THz interferogram along the OX or OY directions is used in order to improve signal-to-noise ratio and suppress speckles in the interference patterns.

In Figure 6f, the dotted line indicates vertical position of the lower interference fringe as a function of temperature. For the empty waveguide, the observed changes in the interference fringe position are due to changes in the guiding properties of the HE₁₁ and HE₂₁ modes. These are mainly due to temperature dependence of the sapphire optical properties, as well as changes in the waveguide geometry with temperature. By contrast, the waveguide containing NaNO₂-layer shows completely

different tendencies in the shift of the interference fringe with temperature, which we attribute to the presence of a NaNO₂ layer and its complex temperature-dependent physical characteristics. Thus, we attribute rapid changes in the position of the lower interference fringe seen at temperatures between 250 and 280 °C (see Figure 6c) to the NaNO₂-film melting ($T_m \equiv 271$ °C). We note that neither optical nor mechanical properties of the sapphire waveguides were changed irreversibly in the course of the high-temperature measurements, thus, the same waveguides could be reused in further measurements after cleaning.^[54]

We believe that the proposed configuration of the THz intra-waveguide interferometric sensor is innovative compared to the other existing intra-waveguide sensor arrangements, as it relies on detection of the amplitude changes in the interference pattern between the two core-guided modes, rather than tracking refractive index changes of a single core-guided mode, as done in other works.^[55–57] The key advantage of our arrangement is that the amplitude sensitive detectors are used to detect phase information via interferogram acquisition. By contrast, intra-waveguide sensors that monitor properties of a single mode have to be phase sensitive in order to match in sensitivity the interferometric methods. Systems based on such phase sensitive detectors/emitters (e.g., TDS-THz) are considerably more expensive than those that employ only amplitude sensitive detection (solid state diodes, Golay cells, etc.). We also note that although we have performed a slow full interference pattern acquisition in our experiments, a practical intra-waveguide interferometry setup would rather use a faster 1D

scan, compressive imaging techniques,^[58] or even a single point measurement to track changes in the fringe position and shape. Finally, we note that although quantitative characterization of the sensitivity of out intra-waveguide interferometric sensor is the subject of additional comprehensive study, nevertheless, the observed significant difference between the temperature dependent interference patterns of the empty waveguide and the waveguide with a NaNO₂ film highlights strong potential of the presented sapphire PC waveguides for high-sensitivity THz sensing in aggressive environments.

6. Discussion

We believe that the sapphire PC waveguides presented in this work could be the prime candidates for various THz sensing applications in aggressive environments. Among these applications, we mention, in particular, the use of sapphire waveguides as hard endoscopes^[12] in the THz medical diagnosis^[7] and therapy,^[9] nondestructive testing of construction materials^[10] with virtually no limitations with respect to temperatures and mechanical loads. For applications in endoscopy, the sapphire waveguide cross-section might need to be modified from what is discussed in this paper in order to reduce the endoscope dimensions, while for other applications, single-mode operation might be a better alternative to a few-mode guidance regime employed by our waveguides. Furthermore, the sapphire shaped crystals could be used as waveguides and cuvettes for studies of condensed matter, gases, plasmas and biological systems^[13,14,16,56,57] using various intra-waveguide sensing modalities.^[55] Finally, they could serve as elements of the imbedded equipment for the THz nondestructive operational control of mechanical systems and products of the petroleum industry,^[15] the open-space research equipment in THz astrophysics,^[17] and the multispectral systems for simultaneous sensing in THz, IR, VIS, and UV ranges. Additionally, due to high hardness of sapphire, the shaped crystals are nonflexible compared to the flexible metal and polymer THz waveguides. Therefore, the sapphire shaped crystals show stability of their guiding properties even in the presence of time-varying mechanical loads and vibrations. This can be of great advantage to the intra-waveguide interferometric sensing, as well as to the accurate broadband remote spectroscopy of the absolute physical constants. All these applications are of high importance to the rapidly developing THz technologies.

The sapphire waveguides are technologically robust as they combine the convenience and advanced performance of the EFG technique with the relatively low material cost and modest fabrication time required to achieve the desired cross-section geometry and waveguide length. Due to mechanical limitations, the EFG-growth setup used in this study can produce shaped crystals with the maximal length of 1 m; however, there are no physical limitations for producing longer waveguides after the appropriate modifications to the crystal growth setup. Additionally, remarkable versatility of the EFG technique^[42] provides rich opportunities for further optimization of the shaped crystal geometry, which could further increase the THz waveguiding performance, achieve the single-, few-, or multimode operation regimes, expand the spectral operation range, reduce the

propagation and coupling losses, as well as reduce or manage the waveguide dispersion. Examining other geometries of the sapphire waveguide cross-section (graded index^[31] or disordered PC lattices,^[33] structures with nonsymmetric channels and thin membranes,^[59] or porous waveguides^[26]) seem to be the promising directions for further research.

7. Conclusions

In this paper, a novel sapphire hollow-core THz PC waveguide was fabricated using EFG shaped crystal growth technique for applications in THz sensing in aggressive environments. We have combined numerical analysis and experimental study to demonstrate that the waveguide operated in the effectively two-mode regime and featured low loss and dispersion. We then applied the developed sapphire waveguide to the high-temperature THz intra-waveguide interferometric sensing of phase changes in the NaNO₂-film. The results of our study confirm strong potential of the sapphire waveguides in various branches of THz science and technology, for which high optical performance and outstanding mechanical, thermal, pressure, chemical, and stress stabilities are required.

8. Experimental Section

EFG Growth of the Sapphire Shaped Crystals: The crystal growth setup uses the 22 kHz induction-heated graphite susceptor with the molybdenum crucible. Using the Verneuil crystal as a feed material, the multichannel sapphire rod is grown from the melt Al₂O₃-film formed on the top of a capillary die at the temperature of 2053 °C and in the ambient high-purity Ar-atmosphere under the pressure of 1.1–1.3 atm. Either a single or a double *c*-axis sapphire seed is used for the growth initiation, while the pulling rate is about 50 mm h⁻¹. During the growth process, the Al₂O₃-melt rises to the top of the capillary die through several 0.25 mm thick ring capillary channels. The crystal shape is mainly determined by the die design, with possible small variations caused by the surface tension of the melt in the meniscus region.

Optical Characterization of the Sapphire Waveguides Using THz-TDS: The THz transmission spectra of the sapphire PC waveguides were acquired using THz-TDS setup operated in the transmission mode. As a source and a detector of the THz pulses, commercial photoconductive antennas from BATOP GmbH based on the low-temperature-grown gallium arsenide (LT-GaAs) were used. The commercial femtosecond fiber laser, used in the setup, features a central wavelength of 0.786 μm, a pulse duration of 93 fs, a pulse repetition rate of 98.59 MHz and an average output power of 68.9 mW. The average power is divided equally between the pump and the probe channels and is slightly attenuated in the optical beam path. As a result, the antenna emitter is pumped, and the antenna detector is probed by the 20 mW laser beams. The optical delay between the pump beam and the probe beam is varied using a 101.6-mm-travel-range double-pass linear mechanical delay stage from Zaber featuring the positioning accuracy of < 3 μm. The THz radiation also undergoes 10 kHz electrical modulation for synchronous lock-in detection of the THz signal. For the waveform detection, the time-domain step of 0.05 ps (to satisfy the Nyquist–Shannon sampling theorem^[60]), the time-domain window size of 100 ps (yielding the frequency-domain resolution of 10 GHz), and the averaging time of 100 ms at each time-domain step with no further waveform averaging were used.

In **Figure 7**, schematic of the THz beam path in the THz-TDS experimental setup is shown, where the emitter detector distance is 45 cm. The emitted THz wave is collimated using a combination

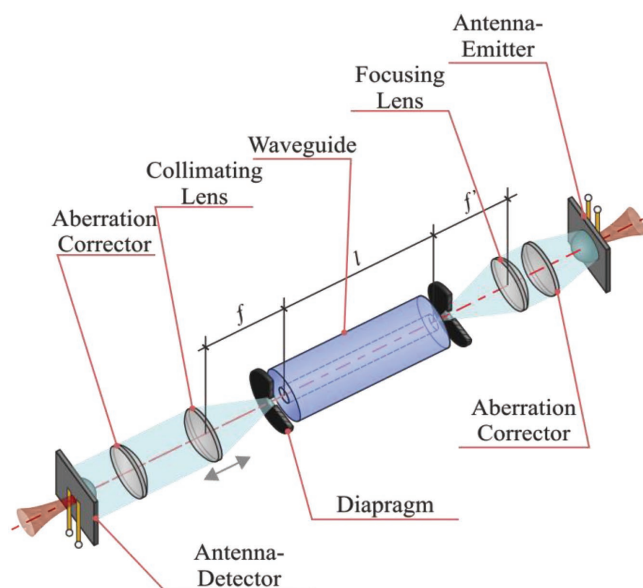


Figure 7. Schematic of the THz beam path in the THz-TDS transmission-mode setup designed for the optical characterization of the hollow-core sapphire THz PC waveguides. All the optical elements in the THz beam path, with an exception of the collimating lens, are rigidly fixed on the optical breadboard, while collimating lens is placed on a rail, thus, capable of accommodating waveguides of different lengths. The input/output diaphragms are mounted directly onto the input/output ends of a test waveguide.

of the high-resistivity float-zone silicon (HRFZ-Si) hemispherical lens, mounted onto an antenna-emitter chip, and the commercial polymethylpentene (TPX) corrector of spherical aberrations, mounted on a separate post, both supplied by the Batop GmbH. The collimated THz beam has a diameter of 25.4 mm. A single planoconvex TPX lens with the focal length of 76.2 mm is used to focus the THz beam with the numerical aperture of $NA \cong 0.16$ onto the 5.5 mm diameter input aperture mounted in front of the waveguide input end. After propagating through the waveguide, the THz beam exits through another 5.5 mm diameter output aperture. The beam is again collimated using another TPX planoconvex lens with the focal length of 76.2 mm. Finally, the beam is focused onto the antenna-detector using an equivalent pair of the TPX aberration corrector and the HRFZ-Si hyperhemispherical lens.

The focusing lens is rigidly fixed, while the collimating lens is mounted on the rail, and can be displaced in order to accommodate waveguides of different lengths. One should mention the importance of using the input/output apertures and the aberration correctors in the optical setup. The apertures allow stabilizing the coupling, and the out-coupling conditions of the THz beam by filtering out contributions of the cladding modes, which is especially important when working with the multimode hollow-core waveguides. The aberration correctors allow achieving high-quality THz beams, which is of particular importance when working with longer THz beam paths that comprise movable optical elements and long waveguide sections.

The reference spectrum was acquired by removing the waveguide and the apertures, while shifting the collimating lens toward the focusing one to form a $1 \times$ telescopic system and placing a 5.5 mm diameter diaphragm at the focal plane between the two lenses. The reference THz signal in frequency-domain features the maximal signal-to-noise ratio of $SNR \cong 5 \times 10^2$ by field, and it allows characterization of the waveguide transmission in the frequency range of 0.2–1.2 THz.

The waveguide measurements were performed at room temperature and ambient humidity (i.e., neither nitrogen gas purging nor vacuum pumping of the sample chamber were used during measurements). Thus, several sharp water vapor absorption deeps in the THz pulse spectra (see Figure 3a) were clearly observed.

THz Intra-Waveguide Interferometric Measurements: Schematic of the THz intra-waveguide interferometric sensor setup is presented in Figure 5. There, a BWO equipped with a wire-grid polarizer is used as a source of the monochromatic linearly polarized THz waves with the electrically tunable output frequency of 0.2 to 0.4 THz. Depending on the value of the output frequency, the output power of the BWO varies in the range of 10^{-2} – 10^{-3} W. For interferometry, the output BWO frequency of 0.355 THz, which corresponds to the electromagnetic wavelength of $\approx 845 \mu\text{m}$, is used. A Golay cell is used as a spectrally nonselective uncooled detector featuring the sensitivity and the time response of $\approx 10^{-5} \text{ V W}^{-1}$ and $\approx 10^{-1} \text{ s}$, respectively. A 22 Hz mechanical chopper is employed for the modulation of the THz beam intensity, which is then detected by the demodulation of the Golay cell signal. To image the THz interference pattern formed at the waveguide output end, raster scanning is performed using detector with a 0.5 mm diameter aperture, which is mounted onto a motorized X–Y translation stage featuring $< 2 \mu\text{m}$ positioning accuracy.

A 150 mm long sapphire waveguide is used as a cuvette to hold the powder. It is mounted inside a temperature cell (an open-air resistance heating furnace) that operates at temperatures ranging from the ambient to $\approx 700 \text{ }^\circ\text{C}$. The THz beam, emitted by the BWO, is first collimated using a teflon lens with the focal length of 50 mm, and, after passing attenuator and mechanical chopper, it is focused onto the input edge of the waveguide using a second equivalent teflon lens (see Figure 5a). The 5.5 mm diameter input diaphragm is mounted at the waveguide input end to prevent excitation of the waveguide cladding modes. The output-diaphragm in the shape of the half-opened disk is mounted at the output end of the waveguide in order to filter out the cladding modes and to enhance the contrast of the resulting interferogram between the “odd” and “even” core guided modes. The resultant interference pattern shows several horizontal stripes and is recorded at a distance of 7 mm from the output end of the waveguide.

Acknowledgements

Numerical analysis and growth of the waveguides were supported by the Russian Science Foundation (RSF), Project # 18-12-00328. Imaging of the interference patterns formed by the two guiding modes was supported by the Russian Science Foundation (RSF), Project # 17-79-20346. Experimental spectroscopic characterization of the guided modes and high-temperature intra-waveguide measurements of the NaNO_2 film were supported by the Russian Foundation for Basic Research (RFBR), Projects # 17-08-00803 and 17-38-80057. M.S. would like to acknowledge Canada Research Chairs Program for its support of the Ubiquitous Terahertz Photonics project. The authors are grateful to Sergey N. Rossolenko and Sergey I. Stolyarov from the Laboratory of Shaped Crystal Growth at ISSP RAS for their help in crystal growth and valuable discussions.

Conflict of Interest

The authors declare no conflict of interest.

Keywords

aggressive environments, edge-defined film-fed growth, photonic crystal waveguides, sapphire shaped crystals, terahertz sensing, terahertz waveguides

Received: May 1, 2018

Revised: August 9, 2018

Published online: September 6, 2018

- [1] S. Lee, *Principles of Terahertz Science and Technology*, Springer, USA 2009.
- [2] P. Shumyatsky, R. Alfano, *J Biomed. Opt.* **2011**, *16*, 033001.
- [3] R. Ulbricht, E. Hendry, J. Shan, T. Heinz, M. Bonn, *Rev. Mod. Phys.* **2011**, *83*, 543.
- [4] B. Yu, F. Zeng, Q. Xing, R. Alfano, *Appl. Phys. Lett.* **2003**, *82*, 4633.
- [5] B. Yu, Y. Yang, F. Zeng, X. Xin, R. Alfano, *Appl. Phys. Lett.* **2005**, *86*, 061912.
- [6] R. Jacobsen, D. Mittleman, M. Nuss, *Opt. Lett.* **1996**, *21*, 2011.
- [7] X. Yang, X. Zhao, K. Yang, Y. Liu, Y. Liu, W. Fu, Y. Luo, *Trends Biotechnol.* **2016**, *34*, 810.
- [8] L. Shi, P. Shumyatsky, A. Rodriguez-Contreras, R. Alfano, *J. Biomed. Opt.* **2016**, *21*, 015014.
- [9] L. Titova, A. Ayesheshim, A. Golubov, R. Rodriguez-Juarez, R. Woycicki, F. Hegmann, O. Kovalchuk, *Sci. Rep.* **2013**, *3*, 2363.
- [10] C. Stoik, M. Bohn, J. Blackshire, *Opt. Express* **2008**, *16*, 17039.
- [11] Y. Shen, T. Lo, P. Taday, B. Cole, W. Tribe, M. Kemp, *Appl. Phys. Lett.* **2005**, *86*, 241116.
- [12] P. Doradla, K. Alavi, C. Joseph, R. Giles, *J. Biomed. Opt.* **2014**, *19*, 080501.
- [13] B. You, J.-Y. Lu, *Opt. Exp.* **2016**, *24*, 18013.
- [14] S. Meier, T. Tsankov, D. Luggenholtscher, U. Czarnetzki, *J. Phys. D: Appl. Phys.* **2017**, *50*, 245202.
- [15] H. Zhan, K. Zhao, H. Zhao, Q. Li, S. Zhu, L. Xiao, *J. Phys. D: Appl. Phys.* **2016**, *49*, 395101.
- [16] N. Laman, D. Grischkowsky, *Appl. Phys. Lett.* **2008**, *93*, 051105.
- [17] S. Withington, *Philos. Trans. R. Soc. A* **2004**, *362*, 395.
- [18] R. McGowan, G. Gallot, D. Grischkowsky, *Opt. Lett.* **1999**, *24*, 1431.
- [19] B. Bowden, J. A. Harrington, O. Mitrofanov, *Appl. Phys. Lett.* **2008**, *93*, 181104.
- [20] K. Wang, D. M. Mittleman, *Nature* **2004**, *432*, 376.
- [21] M. Mbonye, R. Mendis, D. M. Mittleman, *Appl. Phys. Lett.* **2009**, *95*, 233506.
- [22] R. Mendis, V. Astley, J. Liu, D. Mittleman, *Appl. Phys. Lett.* **2009**, *95*, 171113.
- [23] A. Markov, H. Guerboukha, M. Skorobogatiy, *J. Opt. Soc. Am. B* **2014**, *31*, 2587.
- [24] S. P. Jamison, R. W. McGowan, D. Grischkowsky, *Appl. Phys. Lett.* **2000**, *76*, 1987.
- [25] H. Guerboukha, G. Yan, O. Skorobogata, M. Skorobogatiy, *Adv. Opt. Mater.* **2014**, *2*, 1181.
- [26] A. Hassani, A. Dupuis, M. Skorobogatiy, *Appl. Phys. Lett.* **2008**, *92*, 071101.
- [27] A. Hassani, A. Dupuis, M. Skorobogatiy, *Opt. Express* **2008**, *16*, 6340.
- [28] K. Nielsen, H. Rasmussen, A. Adam, P. Planken, O. Bang, P. U. Jepsen, *Opt. Express* **2009**, *17*, 8592.
- [29] B. Ung, A. Mazhorova, A. Dupuis, M. Roze, M. Skorobogatiy, *Opt. Express* **2011**, *19*, B848.
- [30] V. Setti, L. Vincetti, A. Argyros, *Opt. Express* **2013**, *21*, 3388.
- [31] T. Ma, A. Markov, L. Wang, M. Skorobogatiy, *Opt. Express* **2015**, *23*, 7856.
- [32] I. V. Minin, O. V. Minin, V. Pacheco-Pena, M. Beruete, *Appl. Phys. Lett.* **2015**, *106*, 254102.
- [33] T. Ma, H. Guerboukha, M. Girard, A. Squires, R. Lewis, M. Skorobogatiy, *Adv. Opt. Mater.* **2016**, *4*, 2085.
- [34] L.-J. Chen, H.-W. Chen, T.-F. Kao, J.-Y. Lu, C.-K. Sun, *Opt. Lett.* **2006**, *31*, 308.
- [35] J.-T. Lu, Y.-C. Hsueh, Y.-R. Huang, Y.-J. Hwang, C.-K. Sun, *Opt. Express* **2010**, *18*, 26332.
- [36] H. Bao, K. Nielsen, O. Bang, P. U. Jepsen, *Sci. Rep.* **2015**, *5*, 7620.
- [37] H. Han, H. Park, M. Cho, J. Kim, *Appl. Phys. Lett.* **2002**, *80*, 2634.
- [38] M. Skorobogatiy, A. Dupuis, *Appl. Phys. Lett.* **2007**, *90*, 113514.
- [39] A. Argyros, *ISRN Opt.* **2013**, *2013*, 785162.
- [40] S. Atakaramians, S. Afshar V., T. M. Monro, D. Abbott, *Adv. Opt. Photonics* **2013**, *5*, 169.
- [41] D. van Krevelen, K. te Nijenhuis, *Properties of Polymers*, 4th ed., Elsevier, USA **2009**.
- [42] P. I. Antonov, V. N. Kurlov, *Prog. Cryst. Growth Charact. Mater.* **2002**, *44*, 63.
- [43] N. V. Abrosimov, V. N. Kurlov, S. N. Rossolenko, *Prog. Cryst. Growth Charact. Mater.* **2003**, *46*, 1.
- [44] D. Grischkowsky, S. Keiding, M. van Exter, C. Fattinger, *J. Opt. Soc. Am. B* **1990**, *7*, 2006.
- [45] V. N. Kurlov, *Reference Module in Materials Science and Materials Engineering*, Elsevier, USA **2016**.
- [46] K. I. Zaytsev, G. M. Katyba, V. N. Kurlov, I. N. Shikunova, V. E. Karasik, S. O. Yurchenko, *IEEE Trans. Terahertz Sci. Technol.* **2016**, *6*, 576.
- [47] Lumerical Mode Solutions, <https://www.lumerical.com/tcad-products/mode/> (accessed: August 2018).
- [48] S. Johnson, M. Ibanescu, M. Skorobogatiy, O. Weisberg, T. Engeness, M. Soljacic, S. Jacobs, J. Joannopoulos, Y. Fink, *Opt. Express* **2001**, *9*, 748.
- [49] K. Oughstun, N. Cartwright, *Opt. Express* **2003**, *11*, 1541.
- [50] O. Dolgov, D. Kirzhnits, E. Maksimov, *Rev. Mod. Phys.* **1981**, *53*, 81.
- [51] V. N. Kurlov, S. Belenko, *Adv. Mater.* **1998**, *10*, 539.
- [52] K. Ito, T. Katagiri, Y. Matsuura, *J. Opt. Soc. Am. B* **2017**, *34*, 60.
- [53] W. Laue, M. Thiemann, E. Scheibler, K. Wiegand, Nitrates and Nitrites, in: *Ullmann's Encyclopedia of Industrial Chemistry*, Vol. 24, Wiley-VCH, Weinheim **2000**, pp. 149–176.
- [54] D. Zhang, Y. Gan, *Recent Pat. Chem. Eng.* **2013**, *6*, 161.
- [55] M. Skorobogatiy, *J. Sens.* **2009**, *2009*, 524237.
- [56] A. Mazhorova, A. Markov, A. Ng, R. Chinnappan, O. Skorobogata, M. Zourob, M. Skorobogatiy, *Opt. Express* **2012**, *20*, 5344.
- [57] A. Zanishevskaya, A. Shuvalov, Y. Skibina, V. Tuchin, *J. Biomed. Opt.* **2015**, *20*, 040503.
- [58] H. Guerboukha, K. Nallappan, M. Skorobogatiy, *Optica* **2018**, *5*, 109.
- [59] A. Butsch, J. Koehler, R. Noskov, P. Russell, *Optica* **2014**, *1*, 158.
- [60] H. Nyquist, *Trans. Am. Inst. Electr. Eng.* **1928**, *47*, 617.